Chemical Science



EDGE ARTICLE

View Article Online
View Journal | View Issue



Cite this: Chem. Sci., 2025, 16, 13514

dll publication charges for this article have been paid for by the Royal Society of Chemistry

Received 21st April 2025 Accepted 23rd June 2025

DOI: 10.1039/d5sc02883c

rsc.li/chemical-science

Insight into Ni active site coordination in nickel—manganese spinels for methanol electrooxidation catalysis†

Ruiying Guo, a Chunru Liu, a Yun Yang, b *b Shuli Wang and Ligang Feng b *a

As non-precious catalysts, Ni-based catalysts play a significant role in methanol oxidation for energy conversion technologies. At the same time, the effect of the complicated chemical environment on catalytic efficiency remains unclear. Here, the coordination environment of Ni active sites in spinel nickel-manganese (NiMn₂O₄ and MnNi₂O₄) is investigated as a platform to elucidate the correlation with catalytic performance in methanol electro-oxidation. The occupation of Ni²⁺ ions in these structures modulates the intrinsic activity of Ni active sites in NiMn spinels, resulting in different catalytic mechanisms and intrinsic active site efficiency, although they have similar morphology and structure. The high-symmetry NiO₆ octahedral structure in inverse spinel MnNi₂O₄ exhibits superior catalytic performance and stability compared to the NiO₄ tetrahedral structure in normal NiMn₂O₄ spinel. Specifically, at 1.50 V vs. RHE, the MnNi₂O₄ inverse spinel delivers mass activity and specific activity for methanol oxidation that are 1.9 and 3.5 times those of the normal NiMn₂O₄ spinel, respectively. Furthermore, it also maintains a stable current density of 33.5 mA cm $^{-2}$ at 1.56 V vs. RHE for 25 hours. Theoretical calculations reveal that Ni sites in MnNi₂O₄ exhibit a significantly lower activation energy barrier and enhanced CO anti-poisoning capability compared to those in NiMn₂O₄. The Ni sitedependent coordination environment in spinel structures provides useful insights into catalyst development and the methanol oxidation mechanism.

Introduction

Electrocatalytic water splitting holds a pivotal position in sustainable hydrogen generation.¹⁻³ Nevertheless, the oxygen evolution reaction (OER), a multielectron transfer process, suffers from sluggish kinetics and high energy demands.⁴⁻⁶ Recent attention has shifted toward the anodic oxidation of small organic molecules to facilitate hydrogen production, with a particular focus on the methanol oxidation reaction (MOR).⁷⁻⁹ This is mainly due to its low overpotential (0.016 V) and high energy efficiency (~60%), making it a promising alternative.^{10,11}

To fulfil efficient MOR catalysis, attention is directed to nonnoble metal catalysts since platinum group metals (PGMs) are restricted by high cost and susceptibility to CO poisoning. ^{12,13} Ni-based materials, in particular, show great promise as MOR catalysts, including Ni-hydroxides, perovskites, and layered double hydroxides. ^{14,15} During the methanol reaction, the active high-valent NiOOH intermediate is inevitably formed from the

pre-catalyst and serves as a chemical oxidant that converts methanol to carbon dioxide while being reduced to Ni(OH)2.16 Tuning the coordination environment of Ni sites has proven to be an effective strategy to improve catalytic efficiency, as it not only determines the electronic structures of Ni active sites but also governs the reaction mechanisms.17,18 For example, Modoped Ni(OH)2 with ultralow Ni-Ni coordination enhanced the interaction between OH⁻ and CH₃OH at the Ni active center, thereby promoting both the kinetics and durability of methanol electrocatalysis.19 A stable NiSnPH perovskite hydroxide, obtained via selective Sn leaching, optimized the local coordination environment of NiOOH active sites, resulting in enhanced selectivity for methanol oxidation to formate.20 Among Ni-based catalysts, particularly NiMn-based spinel oxides were effective for the MOR due to their stable crystal structures, controllable compositions, and polymetallic synergies.21,22 For instance, multi-walled carbon nanotube (MWCNT)- or reduced graphene oxide (rGO)-supported MnNi₂O₄ showed favourable MOR activity benefiting from the binary transition metal oxides' synergism.23,24 While Ni sites in the spinel structure serve as active sites to trigger methanol oxidation, their precise catalytic mechanism remains unclear. Actually, Ni sites would be an ideal platform to probe intrinsic activity and reveal the effect of the Ni coordination environment in the spinels on catalytic performance. For example, the Ni active sites in spinel nickel-

[&]quot;School of Chemistry and Chemical Engineering, Yangzhou University, Yangzhou 225002, P. R. China. E-mail: ligang.feng@yzu.edu.cn; fenglg11@gmail.com

^bNanomaterials and Chemistry Key Laboratory, Wenzhou University, Wenzhou, P. R. China. E-mail: bachier@163.com

[†] Electronic supplementary information (ESI) available. See DOI: https://doi.org/10.1039/d5sc02883c

Edge Article Chemical Science

manganese (NiO₄ tetrahedral structure for NiMn₂O₄ and NiO₆ octahedral structure for MnNi₂O₄) could be used to elucidate the connection between Ni site coordination and catalytic performance. However, to the best of our knowledge, no relevant reports have specifically addressed this concern.

In this study, we take NiMn-based spinel catalysts (NiMn₂O₄ and MnNi₂O₄) as a platform to explore the correlation between the Ni coordination environment in various spinel structures and catalytic performance for the MOR. MnNi₂O₄ spinel, with Ni sites in an octahedral configuration, exhibits significantly enhanced performance compared to the normal NiMn₂O₄ spinel. Specifically, at 1.50 V vs. RHE, the MnNi₂O₄ inverse spinel delivers mass activity and specific activity that are 1.9 and 3.5 times those of the normal NiMn₂O₄ spinel, respectively. Furthermore, it also maintains a stable current density of 33.5 mA cm $^{-2}$ at 1.56 V vs. RHE for 25 hours. This enhancement stems from the presence of highly active Ni sites in the NiO₆ octahedral coordination environment of MnNi₂O₄, contributing to excellent intrinsic catalytic efficiency. Theoretical analysis demonstrates a lower activation threshold and superior CO anti-poisoning ability of Ni sites in MnNi2O4 compared to NiMn₂O₄. The Ni site-dependent coordination environment in spinel structures provides new insights into catalyst development and the methanol oxidation mechanism.

Experimental

Materials fabrication

In the synthesis of MnNi₂O₄ spinel (Fig. S1†), 1.49 g (5.98 mmol) of Ni(CH₃COO)₂·4H₂O, 1.47 g (5.95 mmol) of Mn(CH₃COO)₂-·4H₂O, and 80 mL of ultrapure water were added into a 100 mL beaker under magnetic stirring. The pH of the solution was adjusted to 10 by the dropwise addition of 5 mol per L NaOH solution, followed by stirring at room temperature for about 15 minutes. Then, the mixture was transferred to a 150 mL Teflonlined autoclave and heated at 150 °C for 12 hours. After natural cooling to room temperature, the synthesized product was collected by centrifuging, washed several times with ultrapure water and anhydrous ethanol, and then dried under vacuum at 60 °C for 8 hours. Finally, the dried powder was annealed in air at 800 °C for 2 hours and cooled to room temperature to obtain MnNi₂O₄ spinel. The NiMn₂O₄ spinel was synthesized by a similar method with different molar ratios of nickel acetate tetrahydrate and manganese acetate tetrahydrate. The NiO and Mn₂O₃ samples were fabricated for performance comparisons (Table S1†).

Materials characterization

The crystal structure was probed using powder X-ray diffraction (XRD) patterns which were obtained on a Bruker D8 Advance with a Cu K_{α} radiation source ($\lambda = 1.5405 \text{ Å}$) under operating conditions of 40 kV and 40 mA, with a scan rate of 5° min⁻¹. The morphology of the NiMn₂O₄ and MnNi₂O₄ spinels was analyzed by using a scanning electron microscope (SEM, Hitachi, S-4800 II, Japan) and transmission electron microscopy (TEM) and high-resolution TEM (HRTEM) measurements (TECNAI G2

operating at 300 kV). The energy-dispersive X-ray detector spectrum (EDS) was obtained on a TECNAI G2 transmission electron microscope equipped with an EDXA detector. The chemical state of the surface was probed using X-ray photoelectron spectroscopy (XPS) with a K_{α} radiation source.

All the electrochemical tests were done using a Bio-Logic VSP electrochemical workstation (Bio-Logic Co., France) in a conventional three-electrode system. The working electrode was obtained by dropping catalyst ink over a glassy carbon electrode (3.0 mm diameter, 0.07 cm²). The catalyst ink was prepared by ultrasonically mixing 4.5 mg of catalyst, 0.5 mg of carbon black, 950 μL of ethanol, and 50 μL of Nafion solution. 10 μL of the catalyst ink was coated over the electrode and dried naturally before electrochemical testing. A graphite rod and saturated calomel electrode (SCE, Hg/Hg₂Cl₂) were used as the counter and reference electrodes, respectively. All the potentials were converted to the reversible hydrogen electrode (RHE).

Cyclic voltammetry (CV) tests were conducted in 1 M KOH solution or 1 M KOH + 1 M CH₃OH solution with a voltage range of 1.06-1.66 V vs. RHE at 50 mV s⁻¹. The electrochemical impedance spectra (EIS) were recorded at frequencies ranging from 1000 kHz to 10 mHz with an amplitude of 5 mV in the above electrode system. The electrochemical surface area (ECSA) was calculated using the redox peak of Ni³⁺/Ni²⁺ in the backward scan of CV curves in the KOH solution. The charge during the cathodic reduction peak of Ni³⁺/Ni²⁺ was calculated using a factor of 0.257 mC cm⁻² (0.257 mC cm⁻² is the charge required to form a monolayer of Ni²⁺). The chronoamperometry (CA) experiment was performed at 1.56 V vs. RHE for 25 hours in 1 M KOH + 1 M CH₃OH solution. The materials, some formulae for the performance calculation, and the theoretical analysis can be found in the ESI.†

Results and discussion

The three-dimensional (3D) spinel structures of NiMn₂O₄ and MnNi₂O₄ are illustrated in Fig. 1a. Both crystallize in the $Fd\bar{3}m$ space group and feature a characteristic structure where metal cations (Ni and Mn) are distributed across tetrahedral and octahedral coordination sites. The coordination structure in these compounds varies slightly with oxidation states due to their mixed valency. In NiMn₂O₄, Ni²⁺ ions typically occupy tetrahedral (A) sites, where each metal ion is coordinated to four oxygen atoms, while Mn3+ ions reside in octahedral (B) sites, coordinated to six oxygen atoms. These metal cations are bridged by oxygen ions (O2-). In the simplified structure, the A sublattice contains Ni²⁺ ions in tetrahedral sites (A), while the B sublattice contains Mn3+ ions in octahedral sites (B). MnNi2O4 adopts a similar spinel-type structure to NiMn2O4 but exhibits an inverse cation distribution because of its different stoichiometry. In this simplified structure, Ni2+ ions preferentially occupy octahedral (B) sites, while Mn4+ ions reside in tetrahedral (A) sites.

During fabrication, as Ni is added, Ni²⁺ ions progressively replace Mn³⁺ ions at octahedral positions, facilitating the formation of the inverse spinel structure. Upon transformation of NiMn₂O₄ into MnNi₂O₄, the MnNi₂O₄ inverse spinel phase

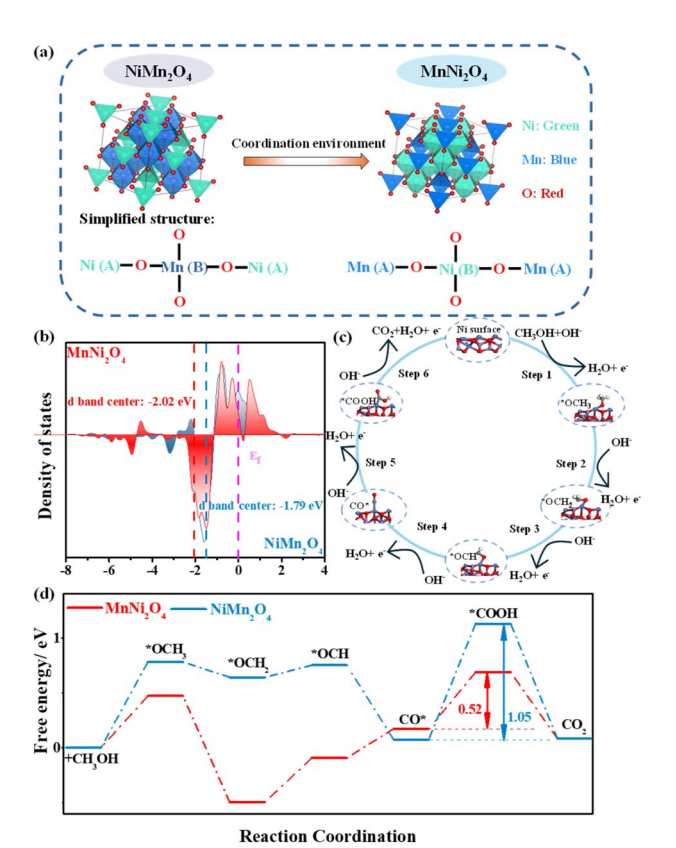


Fig. 1 (a) Structure models of NiMn₂O₄ and MnNi₂O₄ spinels: the transformation of Ni²⁺ from tetrahedral to octahedral coordination. (b) The partial density of states (PDOS) of NiMn₂O₄ and MnNi₂O₄ surfaces. (c) Diagram of the reaction process of the MOR on the MnNi₂O₄–Ni site. (d) The Gibbs free energy diagram for the MOR of NiMn₂O₄ and MnNi₂O₄.

with a high-coordination $\mathrm{NiO_6}$ octahedral structure exhibits enhanced crystal symmetry and stabilizes the spinel structure. Moreover, the increased number of $\mathrm{Ni^{2^+}}$ ions in octahedral geometry generates more active Ni oxidation sites. Conversely, the low-coordination $\mathrm{NiO_4}$ tetrahedral structure in $\mathrm{NiMn_{2O_4}}$ destabilizes the spinel structure. Thus, the occupation of $\mathrm{Ni^{2^+}}$ ions in these structures modulates the intrinsic activity of Ni active sites in NiMn spinels.²⁵

Given the superior MOR performance of $MnNi_2O_4$ to $NiMn_2O_4$ (*vide infra*), density functional theory (DFT) calculations were performed on optimized surface models of Ni and Mn sites in $MnNi_2O_4$ to evaluate the catalytic efficiency of distinct active sites (Fig. S2–S4†).²⁶ Both Ni²⁺ ions preferentially occupied octahedral (B) sites, forming a $Mn^{4+}[Ni_2^{2+}]O_4^{2-}$ valence structure.²⁷ The octahedral NiO₆ structure showed significantly higher MOR performance than the MnO_4 structure, consistent with previous studies (Fig. S5†).²⁸ To elucidate the influence of the Ni site coordination environment on electrocatalytic performance, we compared the Ni d-band centers of $MnNi_2O_4$ and $NiMn_2O_4$. The Ni d-band center in $MnNi_2O_4$ (-1.79 eV), moving further from the Fermi level owing to the robust synergistic effect between Ni d orbitals and O p orbitals

(Fig. 1b). This shift enhances charge transfer efficiency and reduces intermediate adsorption.29 The carbon monoxide intermediate (CO*) adsorption energy (E_{CO*}) is also a key descriptor of MOR catalytic performance. MnNi2O4 exhibited a lower E_{CO^*} value (-1.13 eV) relative to NiMn₂O₄ (-1.24 eV), indicating enhanced CO poisoning resistance capacity (Fig. S6†). The widely accepted mechanism for the MOR catalyzed by Ni-based catalysts follows a stepwise process (Fig. 1c): Ni sites first serve as active centers for methanol adsorption, followed by a sequence of deprotonation steps leading to the formation of multiple bonded intermediates, all of which are formed at Ni sites and eventually convert to CO2.30 The overall MOR pathway can be described as follows: *OCH₃ \rightarrow *OCH₂ \rightarrow *OCH \rightarrow CO* \rightarrow *COOH \rightarrow CO₂. Gibbs free energy analysis revealed that the CO* → *COOH conversion was the ratedetermining step (RDS) in the MOR pathway (Fig. 1d). The energy barrier for this step in MnNi₂O₄ (0.52 eV) was significantly lower than that in NiMn₂O₄ (1.05 eV), indicating more favorable MOR kinetics. Consequently, changes in the coordination environment of Ni active sites not only modulate MOR activation energies but also influence CO poisoning resistance.

The crystal structures of NiMn₂O₄ and MnNi₂O₄ were confirmed by powder X-ray diffraction (XRD), with both

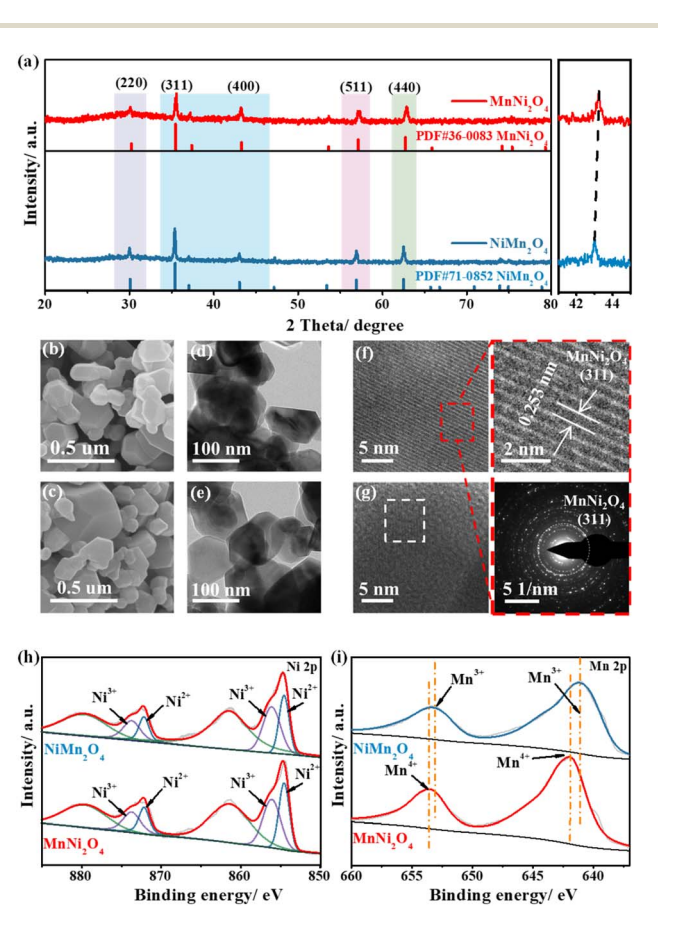


Fig. 2 (a) XRD patterns of NiMn₂O₄ and MnNi₂O₄. (b) SEM image, (d) TEM image, (f) HRTEM image and SAED pattern of MnNi₂O₄. (c) SEM image, (e) TEM image, and (g) HRTEM image of NiMn₂O₄. Ni 2p (h) and Mn 2p XPS spectra (i) of NiMn₂O₄ and MnNi₂O₄.

Edge Article

MnNi₂O₄ spinel (Fig. S8†).

belonging to the face-centered cubic (fcc) structure and $Fd\bar{3}m$ (227) space group (Fig. 2a). The characteristic peaks of MnNi₂O₄ closely resembled those of NiMn₂O₄, but were slightly shifted to high angles at 43.2°, 57.1°, and 62.7°, indicating that Ni²⁺ ions successfully occupied octahedral positions. Scanning electron microscopy (SEM) images revealed that both NiMn₂O₄ and MnNi₂O₄ exhibited irregular aggregated particles (Fig. 2b and c). Transmission electron microscopy (TEM) images showed a similar morphology, with irregular hexagonal planes observed for both samples (Fig. 2d and e). High-resolution TEM (HRTEM) images showed distinct lattice fringes with a *d*-spacing of 0.253 nm, assigned to the (311) planes of MnNi₂O₄ and NiMn₂O₄ spinel structures (Fig. 2f and g). Energy dispersive X-ray spectroscopy (EDS) confirmed the Ni, Mn, C, and O within the samples (Fig. S7†). The elemental mapping images showed

the uniform distribution of Ni, Mn, and O elements in the

Though they have similar morphology and structure, variations in the coordination environment likely alter the chemical states of Ni sites. X-ray photoelectron spectroscopy (XPS) was thus conducted to explore the chemical states. The XPS survey spectra revealed the presence of C, O, Ni, and Mn, with the binding energy calibrated to the C-C bond reference peak at 284.8 eV (Fig. S9†). The high-resolution Ni 2p spectrum displayed two distinct peaks, corresponding to Ni 2p_{1/2} and Ni 2p_{3/2} (Fig. 2h). MnNi₂O₄ showed prominent double peaks of Ni²⁺ located at 854.5 and 872.1 eV, while the weak double peaks at 856.1 and 873.7 eV were attributed to Ni³⁺ (Table S2†). The Ni peak shifted from 854.8 eV in NiMn₂O₄ to 854.5 eV in MnNi₂O₄, indicating that more Ni2+ species occupied the octahedral sites.31 The Ni3+/Ni2+ intensity ratio increased from NiMn2O4 (0.89) to MnNi₂O₄ (1.38), which was attributed to easier surface oxidation and an increased oxidation state at the octahedral sites (Table S2†). For the Mn 2p spectrum, the deconvoluted spectrum of MnNi₂O₄ displayed two major peaks at 644.8 and 656.4 eV, corresponding to Mn⁴⁺, whereas for NiMn₂O₄, the peak positions were shifted to lower energies at 642.7 and 654.3 eV, assigned to Mn³⁺ (Fig. 2i and Table S3†).³² The highresolution O 1s spectrum exhibited three characteristic peaks at 529.8, 531.0, and 532.4 eV, assigned to metal-oxygen bonds, adsorbed hydroxide groups, and adsorbed water molecules, respectively (Fig. S10†).

To investigate the catalytic performance in different coordination environments, electrochemical experiments were conducted on the synthesized catalysts for the MOR. CV measurements of MnNi₂O₄, NiMn₂O₄, NiO, and Mn₂O₃ electrodes in 1 M KOH with and without 1 M CH₃OH indicated that Ni-based electrodes exhibited higher MOR performance, while the Mn₂O₃ electrode showed negligible activity, suggesting that Ni sites served as the active sites for the MOR (Fig. S11†). For MnNi₂O₄, the oxidation peak was assigned to the Ni²⁺/Ni³⁺ redox transition, followed by a rapid increase in the anode current density for both OER and MOR processes (Fig. 3a). The onset potential for the MOR was more negative relative to the OER, and the methanol oxidation closely coincided with the redox peak, while water oxidation occurred after the Ni³⁺ oxidation, suggesting the high energy efficiency of the MOR.³³

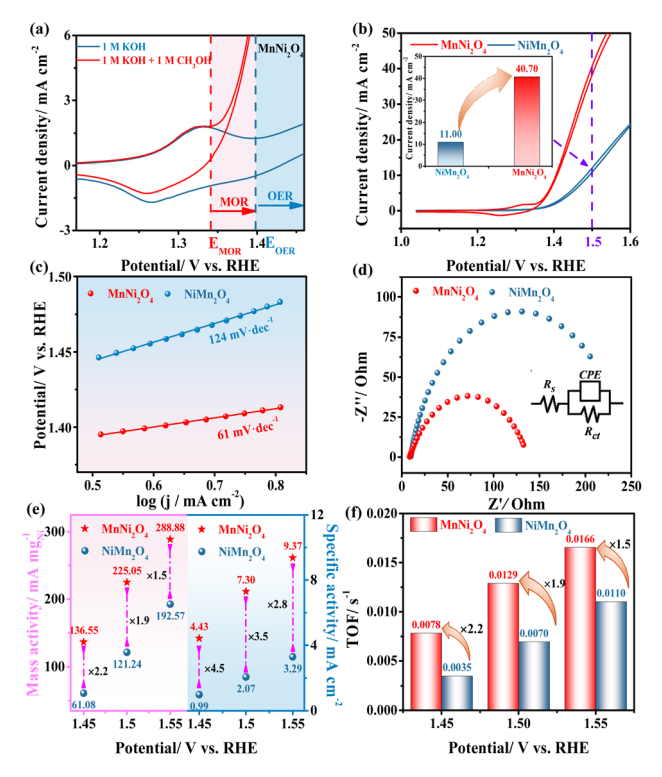


Fig. 3 (a) Cyclic voltammetry curves of MnNi₂O₄ measured in 1 M KOH with and without 1 M CH₃OH at 50 mV s⁻¹. (b) CV curves of NiMn₂O₄ and MnNi₂O₄ measured in 1 M KOH with 1 M CH₃OH at 50 mV s⁻¹ (inset: current density at 1.50 V vs. RHE). (c) Tafel plots of NiMn₂O₄ and MnNi₂O₄. (d) Nyquist plots of NiMn₂O₄ and MnNi₂O₄ at 1.56 V vs. RHE (inset: an equivalent circuit model used for fitting the EIS data). (e) Mass activity and specific activity. (f) TOF of NiMn₂O₄ and MnNi₂O₄ at 1.45, 1.50, and 1.55 V vs. RHE.

By comparing the MOR performance of $MnNi_2O_4$ and $NiMn_2O_4$ electrodes, $MnNi_2O_4$ displayed a much higher forward current density of 40.7 mA cm⁻² at 1.50 V vs. RHE compared to $NiMn_2O_4$ (11.0 mA cm⁻²) (Fig. 3b). Among state-of-the-art non-precious catalysts for methanol oxidation, the $MnNi_2O_4$ spinels ranked the top in their family (Table S4†).

The MOR kinetics were evaluated by using the Tafel slope and electrochemical impedance spectroscopy (EIS). MnNi₂O₄ exhibited a lower Tafel slope of 61 mV dec⁻¹ compared to $NiMn_2O_4$ (124 mV dec⁻¹) (Fig. 3c), indicating different catalytic mechanisms, namely, Eley-Rideal (E-R) and Langmuir-Hinshelwood (L-H) mechanisms, respectively.34 Additionally, the E-R mechanism for the MnNi₂O₄ electrode supported the notion that the absorbed CO* interacted directly with OH- from the alkaline solution and was subsequently oxidized to CO2, which was consistent with the reaction mechanism discussed earlier. The charge transfer resistance (Rct) for the MnNi₂O₄ electrode was 128 Ω , much lower than that of NiMn₂O₄ (253 Ω) (Fig. 3d and Table S5†), indicating faster reaction kinetics due to the highly active octahedrally occupied Ni²⁺ in MnNi₂O₄. The electrochemical stability of the as-prepared catalysts was assessed through a long-term chronoamperometric (CA) test conducted at 1.56 V vs. RHE for 25 hours (Fig. S12†). Initially, the current density of both MnNi₂O₄ and NiMn₂O₄ declined

Chemical Science Edge Article

rapidly due to the diffusion-controlled MOR, but $MnNi_2O_4$ maintained a higher current density of 33.5 mA cm⁻² over time than $NiMn_2O_4$, indicating good stability for the MOR. Moreover, the structure and morphology of $MnNi_2O_4$ catalysts after the stability test exhibited no evident changes, confirming their good anti-corrosion ability for long-term operation (Fig. S13†).

Since MnNi₂O₄ contained two Ni sites, a fair comparison of intrinsic catalytic activity was necessary. To verify the correlation between the oxidation equivalence of Ni active sites and intrinsic catalytic activity for the MOR, commonly used methods for intrinsic activity comparison, including mass activity (MA), specific activity (SA), and turnover frequency (TOF), were employed. By normalizing the current to the Ni mass amount on the electrode, MnNi₂O₄ exhibited enhanced electrocatalytic mass activity compared to NiMn₂O₄ (Fig. S14a†).35,36 The electrochemical active surface area (ECSA) was calculated from the characteristic Ni redox peaks (Table S6†). MnNi₂O₄ showed a higher ECSA value of 0.39 cm² than NiMn₂O₄ (0.37 cm²), indicating slightly greater exposure to active Ni species. More significantly, when normalizing the current to the ECSA, MnNi₂O₄ still showed higher specific activity than NiMn₂O₄ (Fig. S14b†). The typical performance comparison for both mass activity and specific activity at 1.45, 1.50, and 1.55 V vs. RHE is shown in Fig. 3e and Table S6.† Specifically, at 1.50 V vs. RHE, the mass and specific activities of MnNi₂O₄ were 1.9 and 3.5 times those of the NiMn₂O₄ electrode, respectively. Assuming that all the Ni sites were in the active phase, the TOF was calculated (Fig. S15†). At 1.45, 1.50, and 1.55 V vs. RHE, the MnNi₂O₄ electrode exhibited values of 0.0078, 0.0129, and 0.0165 s⁻¹, respectively, about 2.2, 1.9, and 1.5 times those of NiMn₂O₄ (Fig. 3f and Table S7†). These results conclusively showed that Ni sites in MnNi2O4 have significantly higher intrinsic activity than those of NiMn₂O₄.

As mentioned in the above theoretical calculation, the Mn sites are not active for the MOR, but the different Mn oxidation states would influence the performance, as they contribute to the different coordination states of Ni active sites. Additionally, the XPS analysis revealed that the high-valent Mn⁴⁺ in MnNi₂O₄ induced a stronger electronic interaction with Ni sites, promoting the formation of high-valence Ni species and further improving the MOR catalytic performance. Furthermore, it should be pointed out that due to the surface oxidation driven by high potentials, the valence state of Ni sites is increased as can be seen in the Ni redox peaks. In the current study, we revealed the effect of the coordination environment of Ni active sites in nickel-manganese spinels on methanol electrooxidation. It would be more interesting to correlate the surface chemical state changes with the catalytic ability in future studies.

Conclusions

In summary, the Ni active sites in nickel–manganese spinels were probed for methanol oxidation catalysis. Though they have similar morphology and structure, changes in the coordination environment of Ni sites influence their catalytic performance in the MOR. The inverse spinel $MnNi_2O_4$, characterized by Ni

active sites in octahedral coordination, offers a high density of exposed Ni sites with superior intrinsic activity, thereby achieving exceptional catalytic performance and durability. Notably, $MnNi_2O_4$ exhibits mass and specific activities more than twice those of $NiMn_2O_4$. Theoretical calculations reveal a significantly lower activation energy barrier and enhanced CO anti-poisoning capability of Ni sites in $MnNi_2O_4$ compared to $NiMn_2O_4$. The dependence of catalytic efficiency on the coordination environment of Ni sites provides critical insights into the catalytic mechanism of the methanol oxidation reaction.

Data availability

The data supporting this article have been included as part of the ESI.†

Author contributions

Ruiying Guo: conceptualization, methodology, investigation, validation, writing the original draft. Chunru Liu: formal analysis, investigation, validation. Yun Yang: formal analysis, investigation. Shuli Wang: methodology, investigation, and formal analysis. Ligang Feng: writing-review & editing, sources, and funding.

Conflicts of interest

There are no conflicts to declare.

Acknowledgements

This work was supported by the National Natural Science Foundation of China (22272148, and 22202172).

Notes and references

- 1 Y. Guo, X. Zou, X. Wei, W. Bao, J. Zhang, J. Han and F. Jia, *Chin. J. Struct. Chem.*, 2024, 43, 100206.
- 2 C. Liu and L. Feng, Chin. J. Struct. Chem., 2023, 42, 100136.
- 3 A. S. Jamadar, R. Sutar, S. Patil, R. Khandekar and J. B. Yadav, *Mater. Rep.: Energy*, 2024, 4, 100283.
- 4 S. Pan, Z. Yang and F. Luo, *Chin. J. Struct. Chem.*, 2024, 43, 100373.
- 5 S. Pan, Z. Ma, W. Yang, B. Dongyang, H. Yang, S. Lai, F. Dong, X. Yang and Z. Lin, *Mater. Rep.: Energy*, 2023, 3, 100212.
- 6 Y. Lim, S. Surendran, W. So, S. Shanmugapriya, C. Jo, G. Janani, H. Choi, H. S. Han, H. Choi, Y.-H. Yun, T.-H. Kim, M.-J. Kim, K. Jin, J. K. Kim and U. Sim, *Mater. Chem. Front.*, 2023, 7, 5843–5857.
- 7 D. Yan, C. Mebrahtu, S. Wang and R. Palkovits, *Angew. Chem., Int. Ed.*, 2023, **62**, e202214333.
- 8 S. Ali, P. M. Ismail, F. Wahid, A. Kumar, M. Haneef, F. Raziq, S. Ali, M. Javed, R. U. Khan, X. Wu, H. Xiao, G. Yasin, L. Qiao and H. Xu, *Fuel Process. Technol.*, 2022, 236, 107427.

Edge Article Chemical Science

- 9 G. Bharath, G. Karthikeyan, A. Kumar, J. Prakash, D. Venkatasubbu, A. Kumar Nadda, V. Kumar Gupta, M. Abu Haija and F. Banat, Appl. Energy, 2022, 318, 119244.
- 10 J. Li, F. Yang and L. Feng, Coord. Chem. Rev., 2025, 534,
- 11 Y. Kuang, W. Qiao, S. Wang, F. Yang and L. Feng, ACS Mater. Lett., 2024, 6, 1722-1731.
- 12 J. Li, M. Li, F. Yang and L. Feng, Chin. J. Chem., 2025, 43, 146-154.
- 13 M. Li, F. Yang, J. Chang, A. Schechter and L. Feng, Acta Phys.-Chim. Sin., 2023, 39, 2301005.
- 14 H. Cheng, B. Dong, Q. Liu and F. Wang, J. Am. Chem. Soc., 2023, 145, 26858-26862.
- 15 Y. Yi, J. Li and C. Cui, Chin. Chem. Lett., 2022, 33, 1006-1010.
- 16 C. Liu, F. Yang, A. Schechter and L. Feng, Adv. Sens. Energy Mater., 2023, 2, 100055.
- 17 S. Li, R. Ma, J. Hu, Z. Li, L. Liu, X. Wang, Y. Lu, G. E. Sterbinsky, S. Liu, L. Zheng, J. Liu, D. Liu and J. Wang, Nat. Commun., 2022, 13, 2916.
- 18 G. Janani, S. Surendran, D. J. Moon, P. S. Ramesh, J. Y. Kim, Y. Lim, K. Veeramani, S. Mahadik, S. C. Jesudass, J. Choi, I. G. Kim, P. Jung, H. Choi, G. Kwon, K. Jin, J. k. Kim, Y. I. Park, J. Heo, K. Hong, Y. S. Kang and U. Sim, Adv. Sustainable Syst., 2024, 8, 2400059.
- 19 G. Fu, X. Kang, Y. Zhang, X. Yang, L. Wang, X.-Z. Fu, J. Zhang, J.-L. Luo and J. Liu, Nano-Micro Lett., 2022, 14, 200.
- 20 J. Shao, Y. Fang, X. Wu, M. I. Abdullah and Y. Tao, Nano Res., 2024, 17, 2388-2399.
- 21 H. Tian, X. Wang, W. Luo, R. Ma, X. Yu, S. Li, F. Kong, X. Cui and J. Shi, Chem. Sci., 2024, 15, 11013-11020.
- 22 S. Cyril Jesudass, S. Surendran, G. Janani, T.-H. Kim, Y. I. Park and U. Sim, Appl. Surf. Sci., 2025, 688, 162352.

- 23 S. Hosseini, M. B. Askari and H. Beitollahi, Int. J. Hydrogen Energy, 2023, 48, 21240-21248.
- 24 M. B. Askari, P. Salarizadeh, A. Di Bartolomeo and F. Sen, Nanotechnology, 2021, 32, 325707.
- 25 T. Zhang, Y. Liu, L. Tong, J. Yu, S. Lin, Y. Li and H. J. Fan, ACS Nano, 2023, 17, 6770-6780.
- 26 S. Song, X. Huang, Y. Yang and L. Feng, Chem. Commun., 2024, 60, 10906-10909.
- 27 A. B. Devale and D. K. Kulkarni, J. Phys. C: Solid State Phys., 1982, 15, 899.
- 28 M. Ahmad, Q. Riaz, M. Tabassum, S. S. Shafqat, A. t. Ayesha, M. Zubair, Y. Xiong, A. Syed, H. A. Al-Shwaiman, M. A. Nadeem, X. Jia, G. Xu and M. N. Zafar, RSC Adv., 2024, 14, 28285-28297.
- 29 J. Li, C. Wu, Z. Wang, H. Meng, O. Zhang, Y. Tang, A. Zou, Y. Zhang, H. Zhong, S. Xi, J. Xue, X. Wang and J. Wu, Angew. Chem., 2024, 136, e202404730.
- 30 Q. Fang, S. Ye, L. Zheng, H. Wang, L. Hu, W. Gu, L. Wang L. Shi and C. Zhu, ACS Catal., 2024, 14, 9235-9243.
- 31 H.-R. Zhao, C.-Z. Yuan, C. Zhou, W. Zhao, L. Zhang, C.-H. Li, L. Xin, F. Wu, S. Ye, X. Zhang and Y. Chen, J. Energy Chem., 2024, 94, 458-465.
- 32 P. W. Menezes, A. Indra, O. Levy, K. Kailasam, V. Gutkin, J. Pfrommer and M. Driess, Chem. Commun., 2015, 51, 5005-5008.
- 33 T. Wang, L. Miao, S. Zheng, H. Qin, X. Cao, L. Yang and L. Jiao, ACS Catal., 2023, 13, 4091-4100.
- 34 M. Weber-Stockbauer, O. Y. Gutiérrez, R. Bermejo-Deval and J. A. Lercher, Catal. Sci. Technol., 2019, 9, 509-516.
- 35 Y. Liu, L. Bai, Q. Jia, P. Li, Y. Yan, N. Yuan and X. Hao, Chin. Chem. Lett., 2023, 34, 107855.
- 36 J. Li, C. Yin, S. Wang, B. Zhang and L. Feng, Chem. Sci., 2024, 15, 13659-13667.